Analysis of Current Observations on the Georgia Shelf

PIJUSH K. KUNDU

Ocean Sciences Center, Nova University, Dania, FL 33004

JACKSON O. BLANTON

Skidaway Institute of Oceanography, Savannah, GA 31406

MONA M. JANOPAUL

Wave Propagation Laboratory/NOAA, Boulder, CO 80303

(Manuscript received 20 February 1981, in final form 22 May 1981)

ABSTRACT

An analysis is made of HF radar measurements of surface currents in shallow water near the Georgia coast, and also of vertical profile measurements of current and density. The dominant structure is found to be a clockwise ellipse of semidiurnal periodicity, the ellipses becoming smaller, narrower and turning clockwise with depth. There is a definite phase lead of the bottom currents with respect to the upper currents, and some evidence of veering of the currents in the non-Ekman sense. In order to explain the observed vertical variations, a simple analytical expression is developed for periodic rotary currents in a barotropic ocean of constant eddy viscosity and depth h, when the free-surface elliptic motion is known. The solution depends on the ratios ω/f and h/h_{Ekman}, and also on the sense of turning of the free surface ellipse. The model is able to explain several features of the observed vertical variations as frictional effects.

1. Introduction

A new technique of measuring ocean surface currents with high-frequency (HF) radar has been developed by the Sea State Studies Group of the Wave Propagation Laboratory, NOAA, Boulder (Barrick *et al.* 1977). This so-called CODAR (Coastal Ocean Dynamics Applications Radar) can give an estimate of the average surface velocity to a depth of about 1 m with an accuracy of ± 10 cm s^{-1} or better. The estimates are obtained from the Doppler shifts of the reflected waves (Barrick *et al.*, 1977; Barrick 1978). CODAR surface current maps have a grid resolution of 2–3 km for distances up to 40 km offshore; this high spatial resolution of a fairly large coverage area is an important advantage of this technique.

During 9–11 May 1978, an oceanographic experiment was conducted for 48 h on the Georgia shelf in water of 5–17 m depth (Fig. 1). From the CODAR measurements, the surface currents at intervals of 15 min were estimated in a square grid of 256 (16 × 16) points with a grid spacing of 2.4 km, covering a total area of 37 km × 37 km. However, the velocity estimates along the first longshore line of grid points (closest to the coast) are inherently inaccurate (Barrick *et al.*, 1977), and were disregarded in the following calculations.

Simultaneously with these HF radar measurements, vertical profiles of velocity, temperature and salinity were measured from hydrocasts at intervals of 2 h from anchored ships at sites A and B in Fig. 1, by the personnel from the Skidaway Institute of Oceanography (for details see Blanton, 1980). Similar measurements also were made at site D the following year, during November 1979, for five tidal cycles. In addition, during the 1978 experiment the wind was measured at site A, and the currents were also measured at the Savannah Navigational Light Tower (SNLT). Some features of the HF radar measurements and the profiling measurements will be discussed in this paper, and a simple theoretical formulation will be developed to account for the frictional effects.

2. Analysis of data

A plot of the CODAR velocity time series at the various grid points showed that the dominant periodicity was semidiurnal, with a typical amplitude of ± 40 cm s^{-1}. This is also suggested by their spectra (Fig. 2 shows a typical example), although the exact periodicity cannot be ascertained because of poor frequency resolution of these short series. On the basis of historic evidence of current observations on the Georgia shelf (e.g., Haight,

0022-3670/81/081139-11$06.75

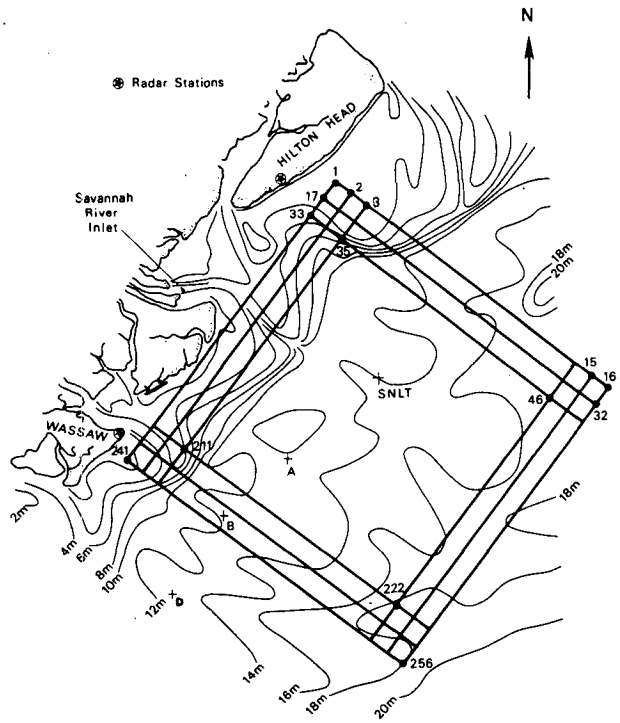

FIG. 1. Location map showing Georgia and South Carolina coasts. The two radar stations are on the Hilton Head and Wassaw islands. A, B and D are anchored ships, and SNLT is the Savannah Navigational Light Tower. The contour interval is 2 m. Only some of the radar grid points (1–256) are indicated.

1942; Redfield, 1958), it will be assumed that the dominant component was the M_2 tide of period 12.42 h.

The mean velocity was found to be an order of magnitude smaller than the velocity fluctuations throughout the region. The large mean northward velocities due to the Gulf Stream are known to be eastward of the region under consideration, at the edge of the shelf break some 130 km from the coast (Lee and Brooks, 1979). A scatter plot of the velocity fluctuations did not show any appreciable polarization of the velocity fluctuations either along or across the isobaths. Although the wind was generally low (<5 m s^{-1}) and did not show any significant correlation with the observed currents, the passage of a weak cold front during the first 24 h correlated with a tendency of the M_2 tidal ellipses to be more alongshore than during the second 24 h.

The water column was stratified, with a vertical density difference of about $1.5\sigma_t$ in a depth of 12 m. Many of the time series of the isopycnal depths (Fig. 3) suggested a vertical movement of the water column phase-locked with the free surface height. Although the isopycnal excursions are not always largest near the top, as would be required of a purely barotropic mode, they are not the highest in the middle of the water column either, as would be required of the first baroclinic mode. However, the flow seems to be composed of more barotropic than baroclinic components.

A plot of the hodograph of the velocity vectors at several grid points suggested clockwise rotation of the velocity vectors. To investigate this further, an analysis of the flow field into the two-dimensional empirical functions was performed, as described in the next section.

3. Empirical orthogonal functions

The use of the so-called Empirical Orthogonal Functions to find the dominant structures in a flow field has become quite common in oceanography (e.g., see Kundu *et al.*, 1975). Given a set of time series, one can find the eigenvalues and eigenfunctions of the matrix of correlation coefficients between the various series pairs. The eigenvalues are the energies in the various modes. If the first few eigenvalues contain most of the total energy, then the first few eigenfunctions are the structures of the dominant modes.

The technique was extended to two-dimensional vectors in Kundu and Allen (1976), where more details can be found. Let u and v be the eastward and northward components of velocity, and

$$w(\mathbf{x}_j, t_\tau) = u(\mathbf{x}_j, t_\tau) + iv(\mathbf{x}_j, t_\tau) \qquad (3.1)$$

denote the two-dimensional (horizontal) velocity

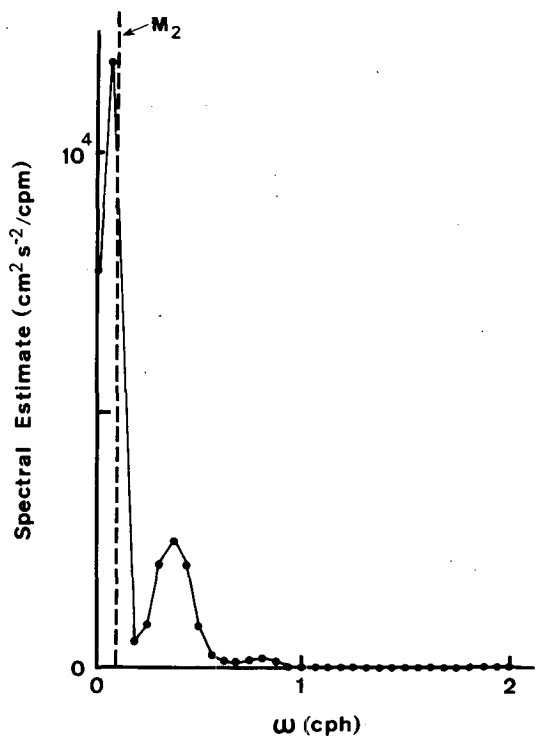

FIG. 2. Spectrum of the v-component at radar grid point 1. The M_2 frequency is indicated. Degrees of freedom = 6.

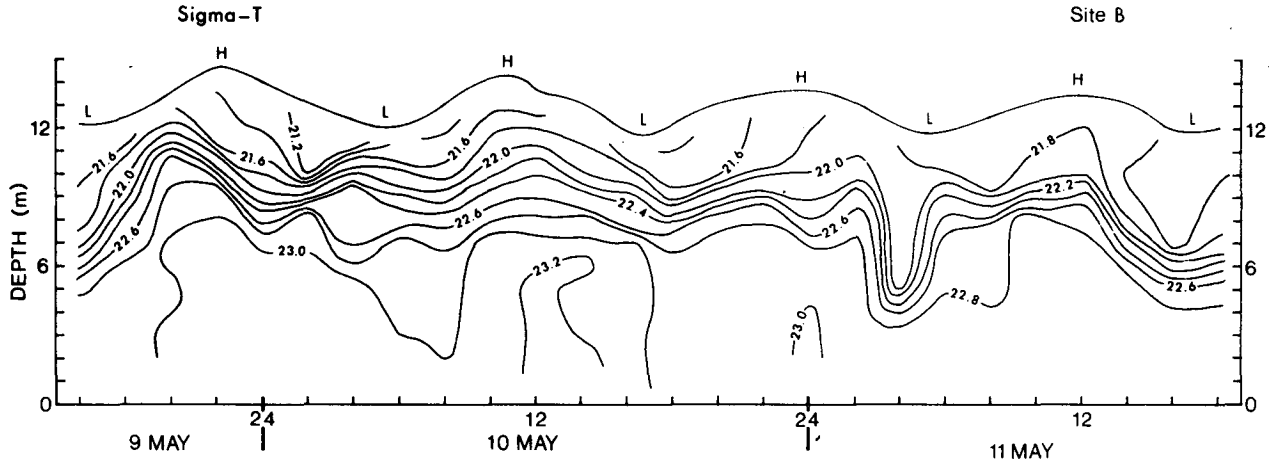

FIG. 3. Time series of isopycnal depths at site B. Times of low and high water at the inlet to the Savannah River are indicated by L and H. (In this figure the depths are indicated from the top, instead of from the bottom.)

vector at time t_τ ($\tau = 1, \ldots, T$) and location $\mathbf{x}_j$ ($j = 1, \ldots, N$), with $i = \sqrt{-1}$. Then a Hermitian matrix of correlation coefficients

$$\mathsf{R}(\mathbf{x}_j, \mathbf{x}_k) = T^{-1} \sum_{\tau=1}^{T} w^*(\mathbf{x}_j, t_\tau) w(\mathbf{x}_k, t_\tau) \quad (3.2)$$

can be determined, where an asterisk denotes the complex conjugate. One can now find the eigenvalues λ_n and eigenfunctions ϕ_n of this matrix:

$$\sum_{j=1}^{N} \mathsf{R}(\mathbf{x}_j, \mathbf{x}_k)\phi_n(\mathbf{x}_j) = \lambda_n \phi_n(\mathbf{x}_k). \quad (3.3)$$

The eigenfunctions are orthogonal to each other, i.e.,

$$\sum_{j=1}^{N} \phi_n^*(\mathbf{x}_j)\phi_m(\mathbf{x}_j) = \delta_{nm}, \quad (3.4)$$

and the data can be expanded in terms of them:

$$w(\mathbf{x}_j, t_\tau) = \sum_{n=1}^{N} E_n(t_\tau)\phi_n(\mathbf{x}_j), \quad (3.5)$$

where the complex amplitudes $E_n(t_\tau)$ are uncorrelated in time

$$\sum_{\tau=1}^{T} E_n^*(t_\tau)E_m(t_\tau) = \lambda_n \delta_{nm}. \quad (3.6)$$

If one orders the eigenvalues (i.e., the energies in the various modes) so that $\lambda_1 > \lambda_2, \ldots, > \lambda_N$, then the first mode is the dominant structure in the data, and $E_1(t_\tau)$ is its time behavior. The technique is especially useful if the first mode explains a large fraction of the total energy, and when assumptions can be made so that the various dynamical factors act independently and produce uncorrelated effects in the data. For example, it is generally found that the baroclinic tides are highly intermittent and have no phase relationship with the barotropic tides (Winant, 1979), so that the effects of the two should be uncorrelated in time. In such a case, a decomposition into the empirical modes would separate the two components. Also, the "noise" will be separated out because it is uncorrelated with any dynamical factors.

Before discussing the results of this modal analysis, a discussion of the correlation coefficient as a function of the distance of separation is useful. Fig. 4 illustrates the correlation function of the CODAR-measured v components, centered in the middle of the flow field, as a function of the distances of separation, both parallel and perpendicular to the coast. The correlation is significant throughout the field, but it is higher for longshore separation. This suggests that the spatial scales perpendicular to the coast are shorter, as has been found in other coastal regions (e.g., Kundu and Allen, 1976). In other words, the flow structures (waves and/or eddies) are elongated in the longshore direction. The magnitude of the correlation also suggests that a decomposition into empirical modes would be useful in this case, since the correlation coefficients are high enough for the concept of "dominant structures" to be meaningful, but they are not so high that the data are already "noise" free.

The eigenvalues and eigenfunctions of the complex matrix R were next computed from (3.2). In order to decrease the size of the matrix, the data from only 36 (6×6) grid points were selected, instead of all the 256 grid points. The selected points were generally separated by 4.8 km, and covered the middle three-fourths of the flow field. It was found that the first mode accounted for 70.0% of the total variance, the second mode explained 9.8% of the variance, and the remaining 34 modes accounted for the rest. The first mode was therefore the dominant structure by far, and Fig. 5 shows the

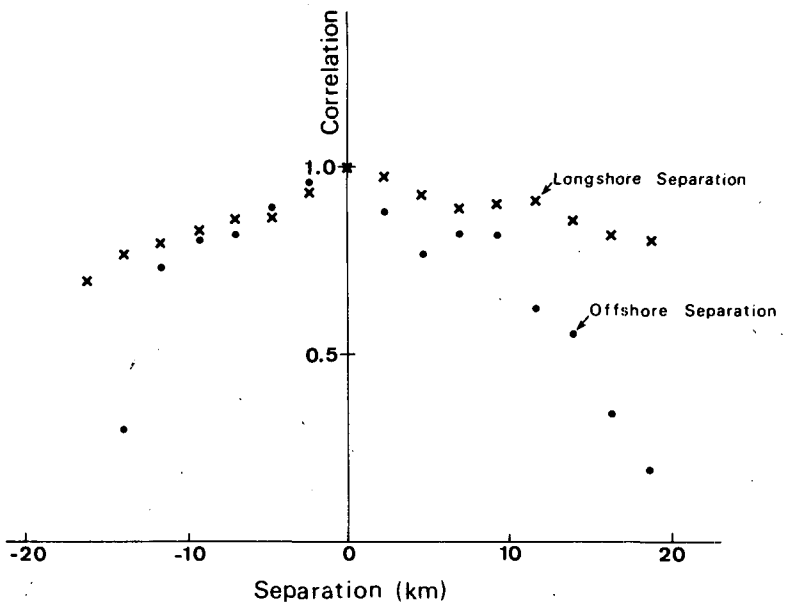

FIG. 4. Correlation coefficients of the v-components of velocity, as a function of the distance of separation. The correlation is centered near the middle of the radar grid. Separations in both alongshore (×) and offshore (●) directions are taken.

structure $\phi_1(\mathbf{x})$ of this mode. [Note that all the arrows in Fig. 5 can be rotated by an arbitrary angle, since $\phi_n(\mathbf{x})$ times a complex number is an eigenfunction if $\phi_n(\mathbf{x})$ is one.] It is apparent that the simultaneous currents of the dominant structure at the various grid points are not very different in magnitude or direction, but there is a tendency for the currents to turn counterclockwise as one goes in a westerly or southwesterly direction through the region. This may be explained by a clockwise rotation of the velocity vector at each point with time, and a westward or southwestward propagation of the oncoming tidal waves. Such a direction of propagation does seem to agree with that given in Redfield (1958), but the speed of propagation suggested in Fig. 5 is about five times that suggested in Redfield. Other probable explanations for the relative orientation of the currents in Fig. 5 are frictional phase differences and bathymetric effects.

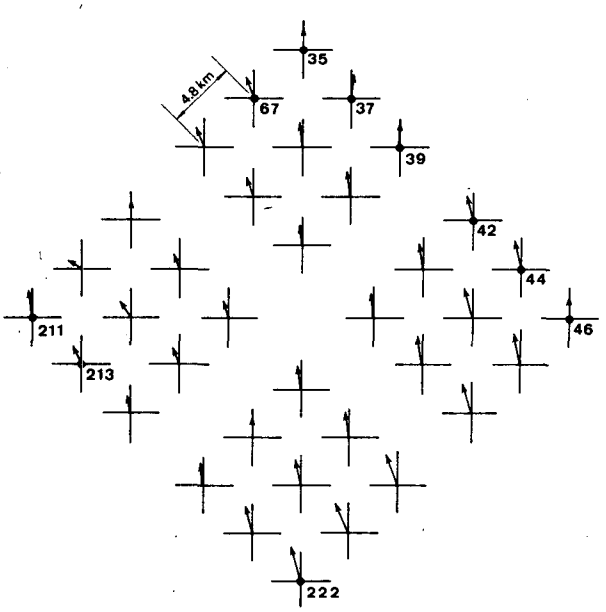

FIG. 5. Map of $\phi_1(\mathbf{x})$, the first empirical orthogonal mode of horizontal currents. Some of the grid points are numbered, and these may be compared with those in Fig. 1. The arrows at each point measure the relative magnitude and direction of the instantaneous currents, with the current at the northernmost grid (grid 35) arbitrarily taken northward. Note that the currents generally rotate slightly counterclockwise as one goes westward or southwestward through the region.

The hodograph plot of the strength of the first mode $E_1(t)$ is shown in Fig. 6 for the first 42 h of the time series. The last 6 h of the times series for $E_1(t)$ behaved less regularly and is not shown. It is seen that the dominant temporal behavior of the flow field is a clockwise ellipse of axes ratio around 1.6–1.9 and periodicity around 12 h. The orientation of the ellipse in this plot is arbitrary because of the arbitrariness in the complex normalization factor in the definition of $\phi_1(\mathbf{x})$. The elliptic hodograph is reminiscent of pure rotational gravity waves of M_2 periodicity without boundary and bottom topographic effects, which would produce clockwise ellipses of axes ratio $\omega/f = 1.83$, taking $2\pi/\omega = 12.4$ h and $2\pi/f = 22.65$ h near the Georgia coast. However, such comparisons may not be very meaningful since boundary, topographic and frictional

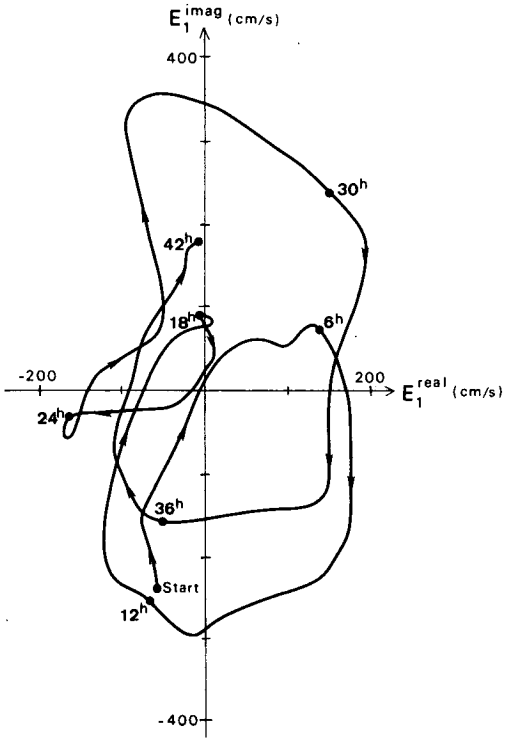

FIG. 6. Hodograph plot of the amplitude $E_1(t)$ of the first empirical mode. The numbers along the hodograph indicate time after starting, at intervals of 6 h. Note the predominant clockwise elliptic motion.

effects are expected to be very important in this region.

4. Frictional effects: A simple model

The vertical profiles of the amplitude and phase of the maximum velocity obtained at sites A, B and SNLT are shown in Fig. 7. It is seen that the currents generally decrease with depth, and that the bottom currents lead the upper currents by ~2 h. The phase lead of the bottom currents is also evident in the contour plots of the velocity components (Fig. 8). In addition, it was observed that the orientation of the elliptic hodograph turns clockwise, looking down (Fig. 9). Much of these facts can be explained as frictional effects, as the following simple calculation shows.

The frictional lead of the bottom currents in an oscillatory flow is a well-known fact, both theoretically and experimentally. Proudman (1953) and Weisberg and Sturges (1976) give solutions with infinite depth and no Coriolis forces, the velocity being linearly oscillatory in contrast to rotary. Fjeldstad (1929), on the other hand, retains the tidal forces and the Coriolis forces, but seems to give a rather complicated, almost incomprehensible solution because of his assumptions that the flow on the upper boundary is unknown. In the present work, the Coriolis forces will be retained, and a very simple solution will be developed by assuming that the flow above the boundary layer describes an elliptic hodograph, which will be regarded as known. This artifact, not used in Fjeldstad (1929), will avoid the solution of the horizontal propagation problem, resulting in considerable simplification.

Using a constant eddy viscosity ν, the linear equations of motion can be written as

$$\frac{\partial w}{\partial t} + ifw - \nu \frac{\partial^2 w}{\partial z^2} = -\frac{\partial p}{\partial x} - i\frac{\partial p}{\partial y}, \quad (4.1)$$

where $w = u + iv$. For simplicity the Coriolis parameter f is taken here as positive. Assuming the hydrostatic condition (long wavelength) and an un-

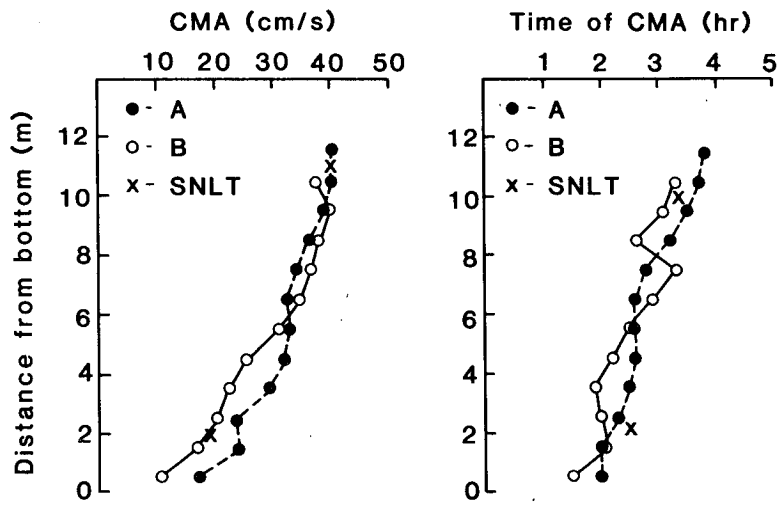

FIG. 7. Amplitude and phase of maximum current, as a function of depth. The phase is given in hours measured from the time of low water. Note the phase lead of the bottom currents. CMA refers to the maximum speed.

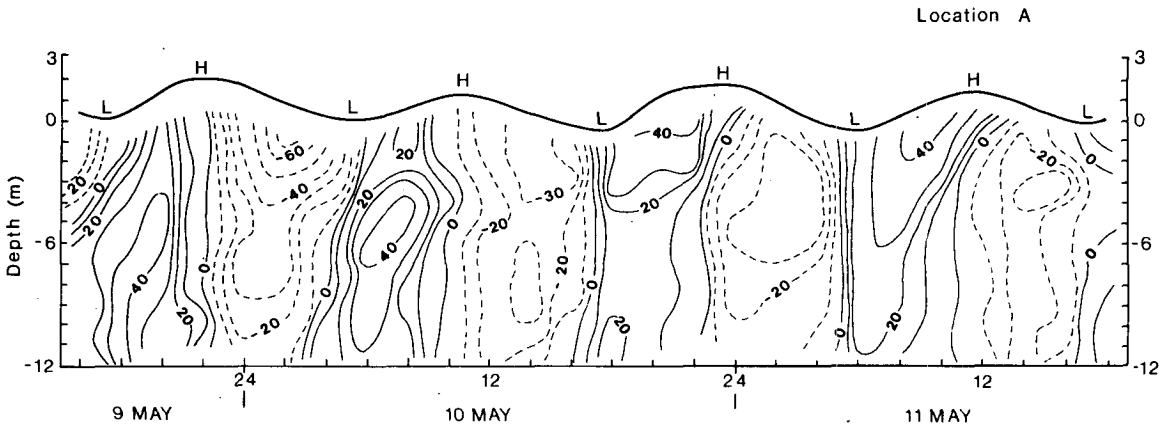

FIG. 8. Contours of the northward velocity component at site A. The dashed lines denote negative values. Note the phase lead of the bottom currents.

stratified fluid, the horizontal pressure gradients can be taken to be independent of z and are imposed by the free-surface height. A no-slip condition is applied at the layer bottom and a no-stress condition is applied at upper surface, where the hodograph of the flow is assumed to be elliptic of frequency ω. The boundary conditions are therefore

$$\left.\begin{aligned} w &= 0 \qquad @ \quad z = 0 \\ \partial w/\partial z &= 0 \qquad @ \quad z = h \\ w &= Ae^{-i\omega t} + Be^{i\omega t} \quad @ \quad z = h \end{aligned}\right\}, \tag{4.2}$$

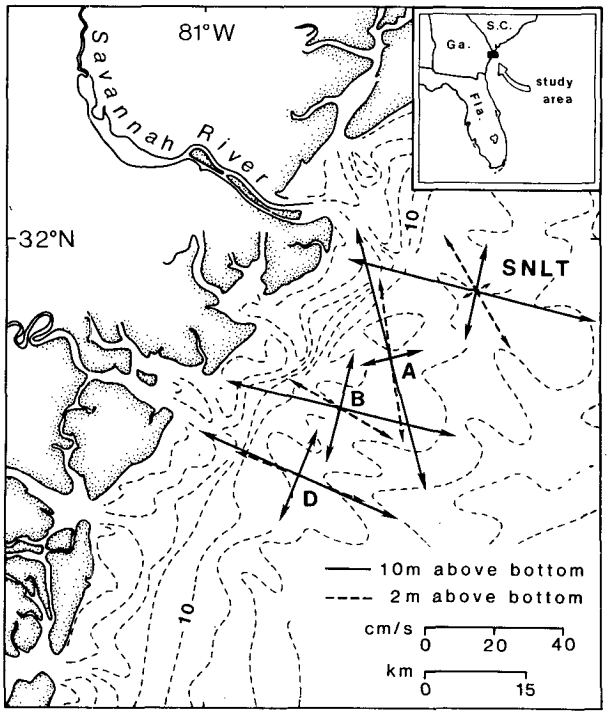

FIG. 9. The principal axes of the elliptic motions at locations A, B and SNLT, for heights $z = 2.0$ and 10.0 m from bottom. Note the clockwise turning of the major axes with depth (looking down).

where the z axis is taken positive upward, and h is the layer depth. The semi-major and semi-minor axes of the free-stream elliptic motion are $(A + B)$ and $|A - B|$, respectively. No generality is lost by taking A, B and ω to be real and positive. The sense of rotation of the ellipse is then negative (clockwise) if $A > B$.

a. Infinite depth

Very simple solutions are obtained by assuming that the depth $h = \infty$. The solution of (4.1), subject to (4.2), can be determined by finding the homogeneous and particular solutions. The pressure gradient is known from the flow at $z = \infty$. The solution is

$$w = Ae^{-i\omega t}(1 - e^{-az}e^{\pm iaz}) + Be^{i\omega t}(1 - e^{-bz}e^{-ibz}), \tag{4.3}$$

where $a = \sqrt{|f - \omega|/2\nu}$ and $b = \sqrt{(f + \omega)/2\nu}$; the positive sign in front of iaz holds if $\omega > f$, and the negative sign if $\omega < f$. Note that both a and b are positive. It is therefore seen that the second part of the solution, multiplied by B, always veers counterclockwise with depth (looking down), that is, in the traditional (steady) "Ekman veering" sense. On the other hand, the first part, multiplied by A, veers in the Ekman sense if $\omega < f$, and in the opposite sense if $\omega > f$. In the present case near the Georgia coast $\omega = 1.83f$, so that $\omega > f$ applies, and $A > B$ because the free stream currents rotate clockwise in time. The first part of the solution (4.3) will therefore be dominant, and the net veering of the currents looking down is expected to be non-Ekman-like. A numerical example given later will verify this.

The times of extrema of velocity are found by setting $d|w|/dt = 0$ in (4.3), which finally gives

$$\omega t = \tfrac{1}{2} \tan^{-1} \frac{2R}{P - Q}, \tag{4.4}$$

where

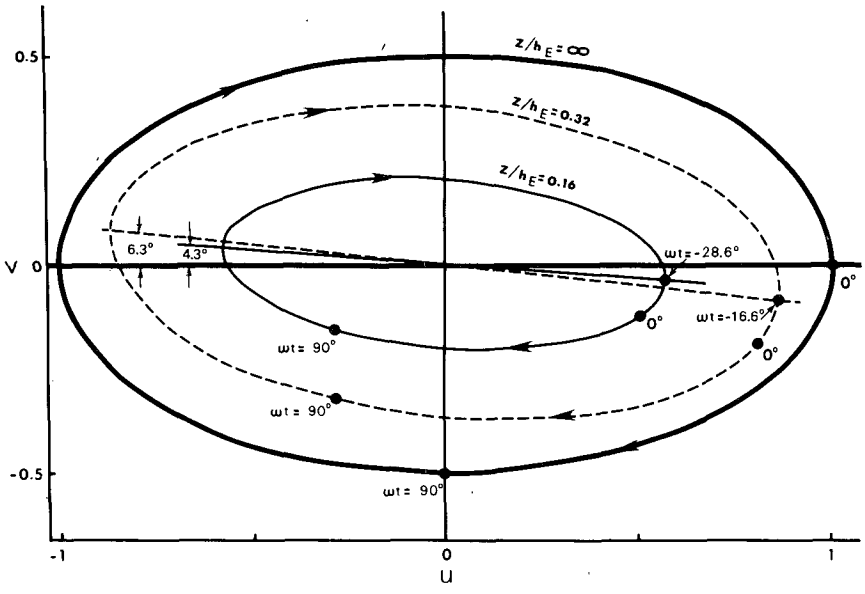

FIG. 10. Theoretical hodographs of the infinite depth solution at heights $z/h_E = \infty$, 0.32 and 0.16, where h_E is the Ekman depth $\pi(2\nu/f)^{1/2}$. The current magnitudes are scaled by its maximum value at $z = \infty$. The points where $\omega t = 0°$ and 90° are marked. The values of ωt at maximum current are 0°, −16.6° and −28.6°, corresponding to $z/h_E = \infty$, 0.32 and 0.16, respectively. The ellipse orientations at the above depths are 0°, −6.3° and −4.3°, respectively. Note the considerable veering of the currents with depth (in a "non-Ekman" sense), a slight turning of the ellipse orientations, and a phase lead of the bottom currents.

$$P = (Ap_1 + Bp_2)^2 + (Bq_2 - Aq_1)^2,$$

$$Q = (Aq_1 + Bq_2)^2 + (Bp_2 - Ap_1)^2,$$

$$R = -(Ap_1 + Bp_2)(Aq_1 + Bq_2) + (Bq_2 - Aq_1)(Bp_2 - Ap_1),$$

$$p_1 = 1 - e^{-\xi}\cos\xi,$$

$$q_1 = e^{-\xi}\sin\xi \quad \text{if} \quad \omega > f$$

and

$$q_1 = -e^{-\xi}\sin\xi \quad \text{if} \quad \omega < f,$$

$$p_2 = 1 - e^{-\eta}\cos\eta,$$

$$q_2 = e^{-\eta}\sin\eta,$$

$$\xi = z(|\omega - f|/2\nu)^{1/2},$$

$$\eta = z[(\omega + f)/2\nu]^{1/2}.$$

The solution (4.3) and some of its properties were numerically evaluated for several specific cases. The first case considered was $\omega = 1.83f$ and clockwise rotation, which would correspond to rotational gravity waves at the M_2 frequency near the Georgia coast. By setting $A = 0.772$ and $B = 0.227$, the maximum velocity at $z = \infty$ (*viz.*, $w_\infty = A + B$) was chosen to be unity, and the axis ratio $(A + B)/(A - B)$ was chosen to be 1.83. These numerical calculations are presented in Figs. 10 and 11. The height z in these figures is expressed in terms of the Ekman depth $h_E = \pi(2\nu/f)^{1/2}$, although a more significant depth scale is probably $\pi[2\nu/(\omega - f)]^{1/2} \approx 1.1h_E$, because of the presence of the $\exp(-az)$ in terms in (4.3).

Fig. 10 describes the hodographs at $z/h_E = \infty$, 0.32 and 0.16. The values of the phase ωt along the hodographs corresponding to the maximum velocity are indicated, and the points corresponding to $\omega t = 0°$ and $\omega t = 90°$ are also marked. It is seen that the maximum velocity is reached at $\omega t = 0°$ for $z/h_E = \infty$, at $\omega t = -16.6°$ for $z/h_E = 0.32$, and at $\omega t = -28.6°$ for $z/h_E = 0.16$. These values, which can be checked by evaluating (4.4), show that the maximum velocity is attained earlier as one goes deeper. The vertical distribution of the magnitude of this phase lead is shown in Fig. 11a. The phase lead of the currents next to the bottom wall with respect to those near the top is ~45°. With depth, the ellipses become smaller (Fig. 11a) and narrower (Fig. 11b).

The solution also predicts that the ellipse orientations change with depth. This is seen in Fig. 10, which shows that the major axis is oriented at 0°, −6.3° and −4.3° for $z/h_E = \infty$, 0.32 and 0.16, respectively. Fig. 11b shows the complete vertical distribution of this major axis orientation, which is seen to reach a minimum value of about −6.5° at $z/h_E \approx 0.4$. Therefore, looking downward, the ellipses first veer clockwise and then counterclockwise with depth.

Note also from Fig. 10 that the simultaneous

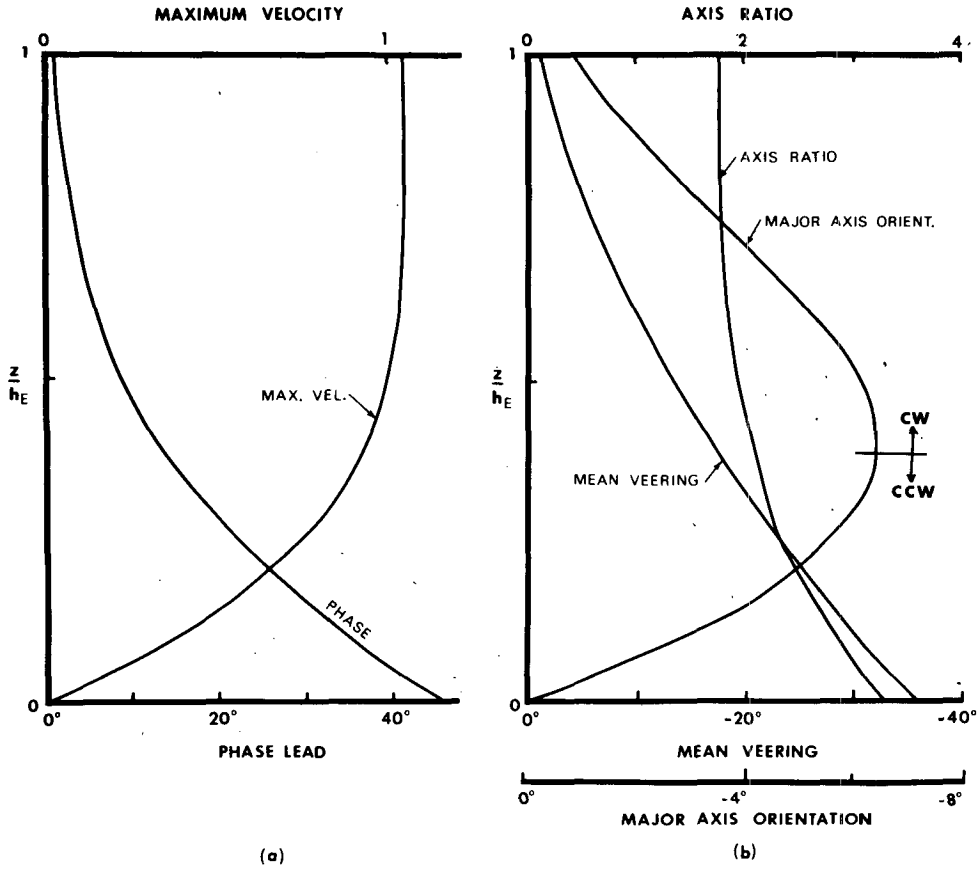

FIG. 11. Vertical distributions of the infinite depth solution. (a) shows the value of the maximum velocity (normalized by its value at $z = \infty$), and its time of occurrence. The sign of ωt at maximum current is negative, and only its magnitude is plotted. (b) shows the major axis orientation, the ratio (major axis)/(minor axis), and the time-mean veering of the currents with respect to the current at $z = \infty$. The mean veering is, in fact, the magnitude of the phase angle of the complex correlation coefficient (4.5).

currents at various depths are oriented at different angles, that is, there is a veering of the current vectors with depth, again caused by friction. The veering seems clockwise looking down, but the magnitude is a strong function of time. This is apparent on comparing the current vectors at the three depths for $\omega t = 0°$ and $\omega t = 90°$. Possibly the best way to compute the time mean veering between two two-dimensional vectors is to compute their complex correlation coefficient

$$\rho = \frac{\langle w_1^*(t) w_2(t) \rangle}{\langle w_1^*(t) w_1(t) \rangle^{1/2} \langle w_2^*(t) w_2(t) \rangle^{1/2}}, \quad (4.5)$$

where $w = u + iv$, and the angle brackets denote time average. The phase angle of the complex number ρ is a measure of the average counterclockwise angle of vector 2 with respect to vector 1, the averaging process being weighted according to the magnitude of the instantaneous vectors. This is explained more fully in Kundu (1976).

The theoretical complex correlation coefficients between the currents at various depths were computed by numerically evaluating (4.5), using the current predicted by (4.3). In the evaluation of ρ, the vector 1 was always taken to be w_∞, so that the phase of $\rho(z)$ is the average counterclockwise veering of vector at z with respect to w_∞. The phase of ρ always came out to be negative, and the magnitude of this phase angle increased with depth (Fig. 11b). This shows that the average frictional veering of the currents with depth is clockwise (looking down), that is, *opposite* to the veering in a steady Ekman layer. It can be shown that this frictional veering in the non-Ekman sense is only possible because $\omega > f$, and because the free-surface ellipse rotates clockwise with time.

The above numerical example holds only for $\omega = 1.83f$ with clockwise rotation (obtained by setting $A = 0.773$, $B = 0.227$); we call this case 1. Three other cases were also numerically evaluated. Although they may not have much relevance to the present observations, a summary of these numeri-

cal results is recorded below, since these cases have relevance for diurnal frequencies, in other regions where f is larger, and where the presence of shallowing topography and coastline may change the direction of rotation of the free surface elliptic motions.

CASE 2: $\omega = 1.83f$, COUNTERCLOCKWISE ROTATION ($A = 0.227, B = 0.773$)

The behavior of the phase lead of bottom currents and change in orientation of the major axis are similar to those in case 1, illustrated in Fig. 11. However, now the axis ratio *decreases* (ellipses getting fatter) with depth, and the mean veering of the current vectors with depth is in the Ekman sense.

CASE 3: $\omega = 0.546f$, CLOCKWISE ROTATION ($A = 0.773, B = 0.227$)

The ellipse orientations veer counterclockwise *rapidly* and monotonically with depth, taking on a *high* value of around 45° near $z = 0$. The ellipses also become narrower with depth. The phase (ωt) for maximum $|w|$ is now small and *positive*. That is, the currents at all z slightly lag those at $z = \infty$. However, unlike cases 1 and 2, the phase lag is zero at $z = 0$ and reaches a maximum value (~6.5°) in the middle of the layer at $z/h_E \approx 0.5$.

CASE 4: $\omega = 0.546f$, COUNTERCLOCKWISE ROTATION ($A = 0.227, B = 0.773$).

The behavior is very much like that in case 3, except that the ellipses become fatter with depth.

b. Finite depth

For finite h, the solution to (4.1) subject to (4.2) is found to be

$$w = A\alpha e^{-i\omega t}\{1 - e^{-az(1\mp i)} + e^{-2ah(1\mp i)}[1 - e^{az(1\mp i)}]\} + B\beta e^{i\omega t}\{1 - e^{-bz(1+i)} + e^{-2bh(1+i)}[1 - e^{bz(1+i)}]\}, \quad (4.6)$$

where

$$\left.\begin{aligned}\alpha &= [1 - 2e^{-ah(1\mp i)} + e^{-2ah(1\mp i)}]^{-1}\\ \beta &= [1 - 2e^{-bh(1+i)} + e^{-2bh(1+i)}]^{-1}\end{aligned}\right\}. \quad (4.7)$$

Here a and b are defined as before; the upper signs in the exponentials apply for $\omega > f$ and the lower signs for $\omega < f$. As before, the pressure gradient has been found from the known flow at $z = h$. Note that, unlike for infinite depth, exponentially increasing terms like e^{az} and e^{bz} are now present, and that $\partial^2 w/\partial z^2 \neq 0$ at $z = h$.

Some important features of the finite depth solution (4.6) are plotted in Fig. 12 for $\omega/f = 1.83$ and clockwise rotation. It is seen that only a small variation of the variables occur across the water column for $h/h_E \leq 0.2$, and that the solution resembles the infinite depth solution for $h/h_E \geq 2.0$. One interesting feature of the finite-depth solution (Fig. 12b) is that the major axis veers first clockwise and then counterclockwise with depth for $h/h_E \geq 1.0$ [ignoring a small (<0.5°) initial counterclockwise turning for $h/h_E \geq 2.0$], whereas the veering is almost uniformly counterclockwise for $h/h_E \leq 1.0$. The ellipses become smaller and narrower with depth for all h/h_E, again ignoring the small variations at large heights for $h/h_E \geq 2.0$.

5. Frictional effects: Comparison with data

The wind speed was quite small (<5 m s^{-1}) during the measurements, both in May 1978 and November 1979. Taking a typical average wind speed as 3 m s^{-1}, the friction velocity corresponding to the surface stress is $u_{*0} = (\tau_0/\rho)^{1/2} = 0.4$ cm s^{-1}. The bottom stress is expected to be less than the surface stress; somewhat arbitrarily using the friction velocity corresponding to the bottom stress to be half of u_{*0}, we take $u_{*_b} \approx 0.2$ cm s^{-1}. It is a reasonable assumption that the friction in this shallow layer behaves like that in the surface layer of a turbulent boundary layer, with a linearly increasing viscosity $\nu(z) \approx 0.4u_{*_b}z$. The depth-average viscosity is therefore $\nu \approx 0.2u_{*_b}h \approx 50$ cm^2 s^{-1} since $h \approx 15$ m. The Ekman depth is then $h_E = \pi(2\nu/f)^{1/2} \approx 30$ m, giving $h/h_E \sim 0.5$. Although the uncertainty in this estimate for h/h_E could be a factor of 2–3, it is instructive to compare the measurements with the $h/h_E = 0.5$ plots of Fig. 12.

It is seen that the phase lead of the bottom currents with respect to those near the top is about 30° for $h/h_E = 0.5$ and about 45° for $h/h_E = 1.0$. These angles are not far from the observed phase lead of 58°, corresponding to the phase lead of 2 h in Fig. 7. The model predicts that the ellipses become smaller and narrower with depth. Fig. 7 shows that the observed currents also decreased with depth, and Fig. 9 shows that the tidal ellipses became narrower with depth. (Note that the minor axes of the tidal ellipses at $z = 2$ m at sites A and B in Fig. 9 are too small to be drawn.)

Observations show that (Fig. 9) the major axis orientation monotonically turns clockwise with depth. Fig. 12b, however, shows that it should turn counterclockwise with depth for $h/h_E < 1.0$. The only way to explain the observed axis veering is to assume that $h/h_E \geq 1.0$. In fact, if the depths corresponding to $z = 2.0$ and 10.0 m are located on the $h/h_E = 1.0$ curve of Fig. 12b, one does find clockwise turning with depth. However, while this can explain the clockwise turning at sites A and B, the turning at site SNLT is too large to be explained by the model.

The model predicts a time-mean veering of the tidal currents in the non-Ekman sense (Fig. 12c).

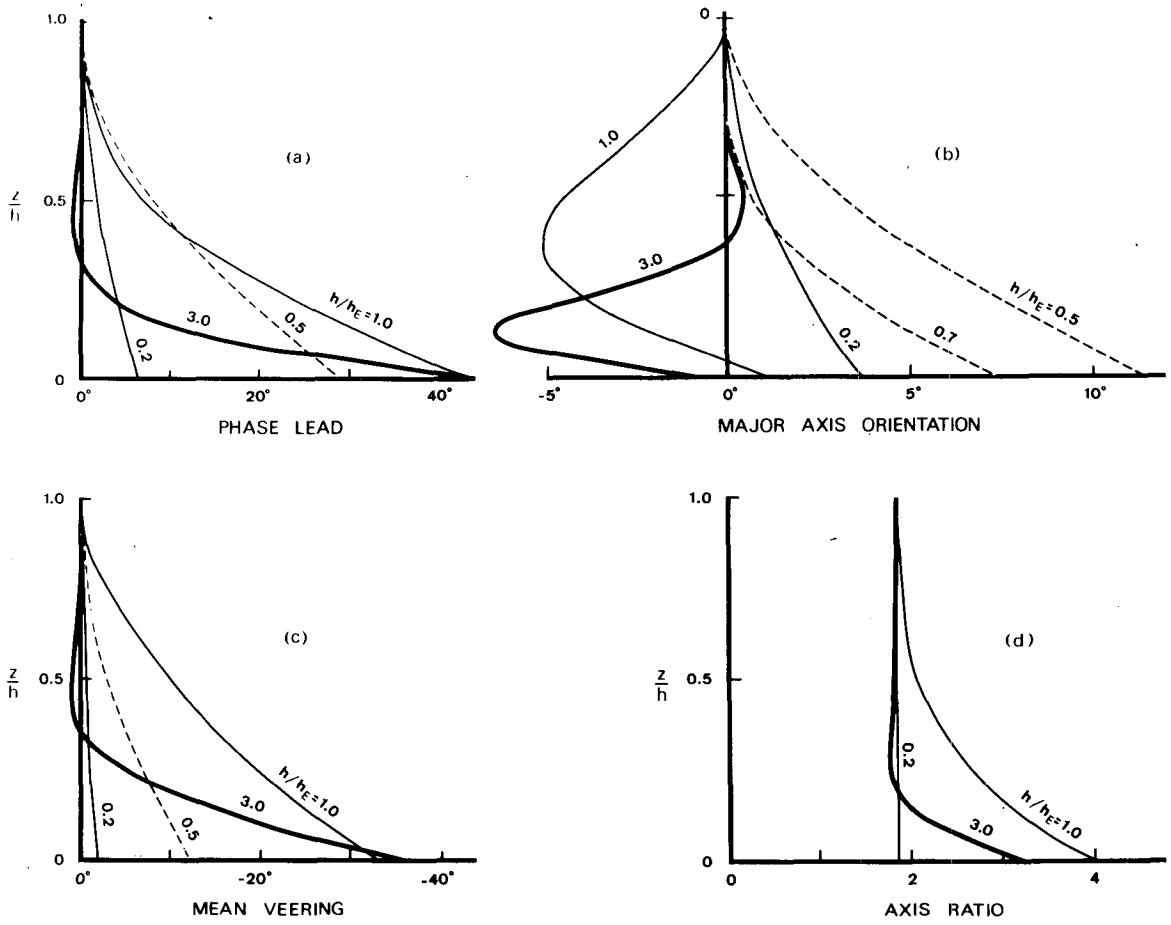

FIG. 12. Vertical distributions of the finite-depth solution for various values of h/h_E.

However, the observations at sites A and B did not show a systematic behavior, which we think is due to a less than satisfactory least-square fit of the tidal currents through the observations. For the 1979 experiment; however, a very good fit was obtained at site D (Fig. 1) between the tidal currents and the data. The mean angles between the current at $z = 10$ m and the deeper currents, calculated from the phase angle of the complex correlation coefficient (4.5), were as follows:

Pair	Angle (deg)
10 m, 9 m	−1.7
10 m, 8 m	−1.5
10 m, 7 m	−1.5
10 m, 6 m	−3.7
10 m, 5 m	−6.1
10 m, 4 m	−8.1
10 m, 3 m	−9.7
10 m, 2 m	−10.7
10 m, 1 m	−7.6

It is seen that these angles all have the right sign, and would fall fairly close to the $h/h_E = 0.5$ curve in Fig. 12c.

In summary, the simple model is able to explain the observed vertical distribution of the tidal current magnitude, axes ratio and phase lead. The agreement of the model with the observed behavior of the veering of the ellipse axes and of the instantaneous currents with depth is somewhat less clear.

6. Summary and remarks

An analysis is made of the HF radar measurements of the surface currents near the Georgia coast at depths 5–17 m. The currents show good correlation in a region 37 km × 37 km. The hodographs of the dominant structure, determined by performing an empirical orthogonal decomposition of the horizontal vector time series, are dominated by semidiurnal clockwise ellipses of axis ratio around 1.6–1.9. The spatial variation of the dominant structure shows that the simultaneous currents turn counterclockwise by 10–20° as one goes westward or southwestward through the region. If this is

due to the effect of the westward propagation of the tidal waves, then the implied phase speeds are about five times those suggested in Redfield (1958); the turning could therefore be due to other reasons, possibly bathymetry or friction.

An analysis also is made of the measurements of the vertical profiles of velocity, temperature and salinity, conducted in the same region simultaneously with the radar measurements. It is found that the currents near the bottom lead those near the top by ~ 2 h, on the average the simultaneous currents veer clockwise with depth (i.e., in the non-Ekman sense), and the current ellipses generally become smaller and narrower with depth while their major axis orientations veer clockwise.

A simple analytical expression is developed for the behavior of periodic rotary currents in a layer with uniform viscosity, for both finite and infinite depths. The depth of the region seems to be about half the Ekman depth h_E. For $\omega > f$, clockwise rotation and $h/h_E \approx 0.5$, the model predicts that the ellipses become smaller and narrower with depth and that their major axes veer counterclockwise with depth. It also predicts that the bottom currents lead the higher currents by about 30° and that there is a time-mean veering of the currents with depth in a sense opposite to that in a steady Ekman layer. The simple constant eddy viscosity theory does agree with several features of the observations.

In the absence of more data, no meaningful discussion of the dynamics of the tidal waves is possible. Tidal charts indicate that the tides in the North Atlantic Ocean off the eastern coast of North America resemble Poincaré waves, describing clockwise ellipses pointed toward the coast, with cotidal lines roughly parallel to the coast. This is unlike the tides off the west coast of the United States, which are dominated by Kelvin waves traveling parallel to the coast (Munk *et al.*, 1970). However, in addition to the frictional effects, the character of these oncoming waves would certainly change drastically due to the presence of the coast and the shallowing of the topography, and edgewave-like effects are expected.

Acknowledgments. Kundu was funded by the Environmental Research Laboratory, NOAA (Contract 04-78-B01-17). Blanton was funded by the U.S. Department of Energy (DE-AS09-HOEV10331) and Georgia Sea Grant College Program, Office of Sea Grant, NOAA (Contract 04-7-158-44126). Janopaul was funded by ERDA (now DOE) under Contract E-(4907)-3204. We thank Drs. Don Barrick and Bob Weber, and other members of the Sea State Studies group, particularly the field crew and those who processed the data, and Drs. J. P. McCreary and S. Y. Chao for discussions.

REFERENCES

Barrick, D. E., M. W. Evans and B. L. Weber, 1977: Ocean surface currents mapped by radar. *Science*, **198**, 138–144.

Barrick, D. E., 1978: HF radio oceanography—a review. *Bound.-Layer Meteor.*, **13**, 23–43.

Blanton, J. O., 1980: Transport of water and salt off the Georgia coast, 9–11 May 1978. Skidaway Institute of Oceanography, Tech. Report, 94 pp.

Fjeldstad, J. E., 1929: Dynamics of free progressive tidal waves. The *Norwegian North Polar Expedition with the "MAUD," 1918–1925, Scientific Results*, Vol. 4, No. 3, Bergen.

Haight, F. J., 1942: Coastal currents above the Atlantic coast of the United States. U.S. Coast and Geodetic Survey, Spec. Publ. No. 230, 73 pp.

Kundu, P. K., 1976: Ekman veering observed near the ocean bottom. *J. Phys. Oceanogr.*, **6**, 238–242.

Kundu, P. K., J. S. Allen and R. L. Smith, 1975: Modal decomposition of the velocity field near the Oregon coast. *J. Phys. Oceanogr.*, **5**, 683–704.

——, and J. S. Allen, 1976: Some three-dimensional characteristics of low-frequency current fluctuations near the Oregon coast. *J. Phys. Oceanogr.*, **6**, 181–199.

Lee, T. N., and D. A. Brooks, 1979: Initial observations of current, temperature and coastal sea level response to atmospheric and Gulf Stream forcing on the Georgia shelf. *Geophys. Res. Lett.*, **6**, 321–323.

Munk, W., F. Snodgrass and M. Wimbush, 1970: Tides off-shore; a transition from California to deep sea waters. *Geophys. Fluid Dyn.*, **1**, 161–235.

Proudman, J., 1953: *Dynamical Oceanography*. Dover, 409 pp.

Redfield, A. C., 1958: The influence of the continental shelf on the tides of the Atlantic coast of the United States. *J. Mar. Res.*, **17**, 432–448.

Weisberg, R. H., and W. Sturges, 1976: Velocity observations in the west passage of Narragansett Bay: a partially mixed estuary. *J. Phys. Oceanogr.*, **6**, 345–354.

Winant, C. D., 1979: Coastal current observations. *Rev. Geophys. Space Phys.*, **17**, 89–97.